RSC Advances

PAPER

View Article Online
View Journal | View Issue

Cite this: *RSC Adv.*, 2025, **15**, 28428

Dual-mode optical thermometry based on up- and down-conversion photoluminescence in $LiCaLa(MoO_4)_3:Er^{3+}/Yb^{3+}$ phosphors with high sensitivity

Ikhlas Kachou,[a] Yosra Bahrouni,[a] Kamel Saidi,[ab] Mohamed Dammak,*[a] Irene Mediavilla[c] and Juan Jiménez[c]

The integration of down-conversion (DC) and up-conversion (UC) photoluminescence mechanisms has attracted significant attention for applications in optical thermometry and solid-state lighting. Combining both emission processes within a single material enables dual-mode temperature sensing, offering enhanced flexibility and precision. In this study, we report a pioneering investigation of the dual-mode thermometric performance of $LiCaLa(MoO_4)_3$ phosphors co-doped with Er^{3+} (0.02) and Yb^{3+} (0.15), synthesized *via* a solid-state reaction route. To the best of our knowledge, this is the first report demonstrating simultaneous DC and UC-based thermometric behavior in this host matrix. The structural and morphological features of the synthesized phosphors were characterized by X-ray diffraction (XRD) and scanning electron microscopy (SEM), while their optical properties were analyzed using photoluminescence (PL) spectroscopy. XRD patterns confirmed the formation of a pure monoclinic $LiCaLa(MoO_4)_3$ phase. Under UV excitation at 325 nm, green DC emissions from Er^{3+} ions were observed, whereas intense green UC luminescence was recorded under 980 nm near-infrared excitation. Co-doping with Yb^{3+} significantly enhanced both DC and UC emission intensities. A dual-mode optical thermometry approach was implemented using non-thermally coupled levels (NTCL) of Er^{3+}, enabling simultaneous temperature evaluation from both DC and UC emissions. At 300 K, the relative sensitivities (S_r) reached 1.2% K^{-1} for DC and 2.1% K^{-1} for UC modes. At elevated temperatures (510 K), the maximum absolute sensitivities (S_a) were 13.6 × 10^{-3} K^{-1} (DC) and 25 × 10^{-3} K^{-1} (UC), respectively. The system demonstrated good temperature resolution, with uncertainties (δT) below 0.313 K, confirming its potential for precise and robust optical temperature sensing.

Received 18th July 2025
Accepted 6th August 2025

DOI: 10.1039/d5ra05181a

rsc.li/rsc-advances

Introduction

The rapid development of modern technology has led to growing interest in luminescent materials doped with rare earth ions (RE^{3+}), owing to their unique optical and magnetic properties. These materials are promising candidates for a wide range of practical applications, including up-conversion (UC) and down-conversion (DC) luminescence, solid-state lasers, optical fibers, and advanced magnetic devices.[1–3] In particular, rare-earth-based UC nanocrystals have recently attracted significant attention in the field of biological imaging due to their high photostability, sharp emission bands, and deep tissue penetration.[4,5]

Previous studies have predominantly focused on temperature sensing based on either UC or DC mechanisms individually. However, few reports have explored the simultaneous utilization of both UC and DC processes for temperature measurements, despite the potential advantages of such dual-mode thermometry.[6,7] UC luminescent materials are of particular interest for optical thermometry because temperature variations can be monitored by analyzing the fluorescence intensity ratio (FIR) between emissions originating from thermally coupled levels (TCLs) of lanthanide ions.[8,9] The FIR method is typically applied using emission bands separated by an energy gap ranging from 200 to 2000 cm^{-1}, a range well-matched by lanthanide ions such as Er^{3+}, Ho^{3+}, Nd^{3+}, Pr^{3+}, and Dy^{3+}, which have been widely employed as FIR-based optical thermometers.[10,11]

Among these, Er^{3+} is particularly suitable due to its rich energy-level structure and strong green emissions originating

[a]*Laboratoire de Physique Appliquée, Faculté des Sciences de Sfax, Département de Physique, Université de Sfax, BP 1171 Sfax, Tunisia. E-mail: madidammak@yahoo.fr; mohamed.dammak@fss.usf.tn*

[b]*Department of Physics, Sfax Preparatory Engineering Institute, University of Sfax, 1172-3000 Sfax, Tunisia*

[c]*GdS Optronlab, Department of Condensed Matter Physics, University of Valladolid, LUCIA Building, Paseo de Belen 19, Valladolid, 47011, Spain*

from the thermally coupled $^2H_{11/2}$ and $^4S_{3/2}$ levels. These emissions are highly sensitive to environmental temperature and can be excited *via* both UC and DC mechanisms.[12] However, Er^{3+} suffers from a low absorption cross section in the near-infrared (NIR) region, which limits its excitation efficiency under NIR light. To overcome this limitation, Yb^{3+} is frequently used as a sensitizer due to its strong absorption around 980 nm and its efficient energy transfer to Er^{3+}. Co-doped Yb^{3+}/Er^{3+} systems have shown enhanced green UC emissions and have been extensively investigated for various applications.[13]

Despite these advancements, further studies are still needed to optimize the doping concentrations and emission stability of Yb^{3+}/Er^{3+}-activated phosphors.[14,15] The simplified energy level scheme and large absorption cross section of Yb^{3+} make from it an ideal sensitizer for improving the UC luminescence and, consequently, the temperature sensing performance of Er^{3+}-based phosphors.[16]

Dual-mode fluorescence thermometry, which combines both downshifting (DS) and upconversion (UC) emission within a single host matrix, offers significant advantages for practical temperature sensing. DS mode, typically excited by UV light, benefits from efficient excitation *via* host-sensitized pathways (*e.g.*, $MoO_4^{2-} \rightarrow Ln^{3+}$) and is well-suited for near-surface temperature detection. In contrast, UC mode, excited by NIR radiation, enables deeper light penetration, reduced background fluorescence, and remote sensing capabilities, making it ideal for biomedical and high-temperature environments. Integrating both modes in a single material enhances operational versatility, expands the measurable temperature range, and improves adaptability across diverse sensing scenarios. In this context, tungstate and molybdate hosts have gained increasing attention for their favorable optical characteristics, including efficient luminescence, low phonon energy, and chemical durability, making them good candidates for optical thermometry applications. These hosts support strong 4f–4f transitions of rare-earth dopants while minimizing non-radiative losses due to multiphonon relaxation, which is crucial for enhancing both DC and UC emissions.[17–20]

Among various host matrices, the molybdate compound $LiCaLa(MoO_4)_3$ with a scheelite-type structure has emerged as a promising host material due to its high chemical and thermal stability, low phonon energy, and relatively low synthesis temperature.[20]

Recent studies have explored its optical properties, including emission spectra, luminescence mechanisms, and fluorescence lifetimes, mainly for solid-state lighting and white light-emitting diode (LED) applications.[21,22] However, its potential in optical temperature sensing remains largely unexplored.

Given its stability and strong upconversion (UC) emission properties, $LiCaLa(MoO_4)_3$ is a promising candidate for non-contact optical thermometry. Optical temperature sensors based on photoluminescence offer several advantages, including fast response time, high spatial resolution, and real-time monitoring capabilities. Therefore, investigating the thermometric performance of $LiCaLa(MoO_4)_3$ phosphors is both timely and scientifically relevant for the development of advanced optical sensing technologies.

Although Er^{3+} ions are widely used in temperature-sensitive luminescent materials due to their $^2H_{11/2}$ and $^4S_{3/2}$ levels,[23] their weak infrared absorption limits UC efficiency under NIR excitation. In contrast, Yb^{3+} can efficiently absorb NIR light and transfer the energy to Er^{3+}, enhancing the UC luminescence. Thus, co-doping Er^{3+} and Yb^{3+} into the $LiCaLa(MoO_4)_3$ matrix can significantly improve its luminescent properties and its overall temperature sensing performance.[24]

In this work, we aim to explore the optical thermometric performance of $LiCaLa(MoO_4)_3$ phosphors co-doped with Er^{3+} and Yb^{3+} ions by simultaneously employing both up-conversion (UC) and down-conversion (DC) photoluminescence mechanisms. The phosphors were synthesized *via* a conventional solid-state method and characterized using XRD, SEM, and PL spectroscopy to evaluate their structural, morphological, and optical properties. A dual-mode optical temperature sensing strategy was implemented based on non-thermally coupled levels (NTCL) of Er^{3+}, under both UV and NIR excitations. In the following sections, we will detail the experimental methods, analyze the temperature-dependent emission behavior, and assess the relative and absolute sensitivities, as well as the temperature resolution of the system. These findings are will highlight the potential of $LiCaLa(MoO_4)_3$:Er^{3+}/Yb^{3+} as an efficient dual-mode optical thermometer for future applications in advanced thermal sensing technologies.

Experimental section

Raw materials and preparation methods

LCLMO:0.02 Er^{3+}/0.15 Yb^{3+} phosphor was obtained by a conventional high-temperature solid-state reaction method in air atmosphere. Analytical grade MoO_3 (99.99%), $LiCO_3$ (99.99%), $CaCO_3$ (99.99%), $LaCO_3$ (99.99%), Er_2O_3 (99.99%) and Yb_2O_3 (99.99%) were used as raw materials. In a standard synthesis, stoichiometric amounts of raw materials were first weighed and well mixed in an agate mortar. The uniform mixtures were then placed in alumina crucibles and calcined in a high-temperature resistant furnace at 800 °C for 5 hours. The final products were then produced by allowing the furnace to cool naturally to room temperature. Finally, the phosphors obtained were ground to suit the spectral measurement requirements.

In this work, the doping concentrations of 15 mol% Yb^{3+} and 2 mol% Er^{3+} were selected based on previous literature as an effective combination to achieve strong upconversion (UC) under 980 nm excitation and downshifting (DS) luminescence under 325 nm excitation. This composition provides a good balance between emission intensity and stability, ensuring reliable performance for optical thermometry without the need for further optimization.[25,26]

Characterization

X-ray diffraction (XRD) was employed to verify the crystal line structure and phase purity of the samples. The morphology and microstructures of the phosphors were analyzed by scanning electron microscopy (SEM) taken on a Hitachi SU-4800 field

emission. UV-vis-NIR absorption spectra were recorded on a PerkinElmer Lambda 365 spectrophotometer and photoluminescence (PL) spectra were recorded as a function of temperature using a Labram UV-HR 800 Raman spectrometer from Horiba-Jobin Yvon.

Results and discussion

Phase and morphology

In order to clarify the crystallinity and phase composition of the LCLMO:0.02 Er^{3+}/0.15 Yb^{3+} phosphors, the X-ray diffraction (XRD) profiles are shown in Fig. 1a. The diffraction peaks found in the samples were in close agreement with the standard positions identified for $LiCaLa(MoO_4)_3$ standard maps (JCPDS # 29-0351),[27] confirming that the introduction of rare earth ion doping did not change the phase structure of the sample. Rietveld refinement was performed to refine the crystallographic parameters as shown in Fig. S1. The optimized unit cell dimensions are: $a = b = 5.24741$. Å, $c = 11.47538$ Å, and the unit cell volume = 315.978 $Å^3$. The refinement confirms a pure tetragonal phase with R-factors (R_{wp} = 11.22%) indicative of a high-quality fit. No detectable impurities or structural defects were observed, corroborating the effectiveness of the solid-state synthesis route.

The doping of Er^{3+} ions does not impact the parent phase of LCLMO, thus specifying the appropriate doping of Er^{3+}/Yb^{3+} ions at the lattice sites of one of the host cations, La^{2+}, Li^{+}, Mo^{4+} or Ca^{2+}. The possible doping position of the Er^{3+}/Yb^{3+} ions can be obtained by comparing the ionic radius difference (D_r) of the host cations with the dopant ions, which can be estimated as follows:[28]

$$D_r = \frac{R_s - R_d}{R_s} \times 100\% \quad (1)$$

where D_r is the percentage difference in radius. R_s and R_d denote the radii of the substitution ions and the dopant ions, respectively. The dopants (Er^{3+} and Yb^{3+}) are considered to be taking over the sites of the La^{3+} ions in the LCLMO host lattice, given the effective ionic radii and the charge balance of the cations. Using eqn (1), the D_r values of La^{3+}/Er^{3+} and La^{3+}/Yb^{3+} were calculated to be 13, 75% and 15, 89%, respectively. These determined D_r values indicate that Er^{3+} and Yb^{3+} ions can easily enter the LCLMO host lattice by substituting La^{3+} ions, as the D_r values are much below 30%.

The morphological characteristics of the LCLMO:0.02 Er^{3+}/0.15 Yb^{3+} sample, studied by SEM are shown in Fig. 1b showed that the powders obtained had a uniform white color, with grain sizes around 1 μm, forming some agglomerates by coalescence. Generally, the particles are very closely packaged, which reduces the light scattering and thus contributes to higher luminescence efficiency.

UV-visible spectroscopy analysis

Fig. S2 displays the UV-vis-NIR diffuse reflectance spectra of LCLMO:0.2 Er^{3+}/0.15 Yb^{3+}. The LCLMO:0.2 Er^{3+}/0.15 Yb^{3+} sample exhibits strong host absorption in the UV region, centered at 313 nm, which is attributed to the charge transfer band (CTB) of Mo–O. In addition to these broad CTB bands, several peaks are observed at 522 nm, 654 nm, and 800 nm, corresponding to the transitions from the ground state $^4I_{15/2}$ to various excited states, namely $^2H_{11/2}$, $^4F_{9/2}$, and $^4I_{9/2}$ of Er^{3+} ions, respectively, as shown in Fig. S2. The absorption peak around 980 nm is assigned to the $^2F_{7/2} \rightarrow {}^2F_{5/2}$ transition of the Yb^{3+} ion.[29]

DC luminescence properties

In order to investigate the photoluminescence emission characteristics, the samples were excited with a He–Cd laser (325 nm). The emission spectra shown in Fig. 2a consist of several peaks at 526 nm, 546 nm and 660 nm, which are assigned to the $^2H_{11/2} \rightarrow {}^4I_{15/2}$, $^4S_{3/2} \rightarrow {}^4I_{15/2}$ and $^4F_{9/2} \rightarrow {}^4I_{15/2}$ transitions of

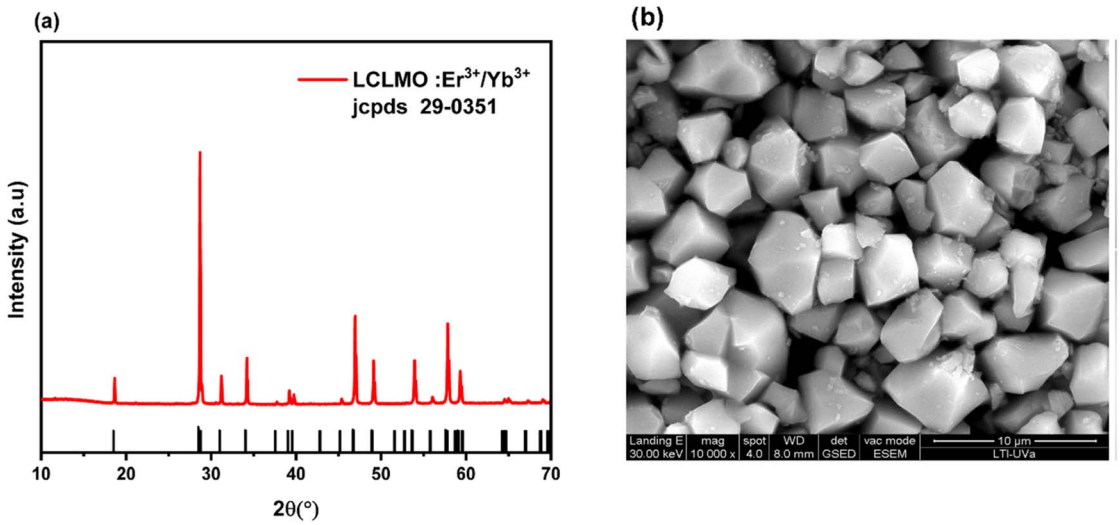

Fig. 1 (a) X-ray powder diffraction patterns, (b) SEM of LCLMO:Er^{3+}/Yb^{3+}.

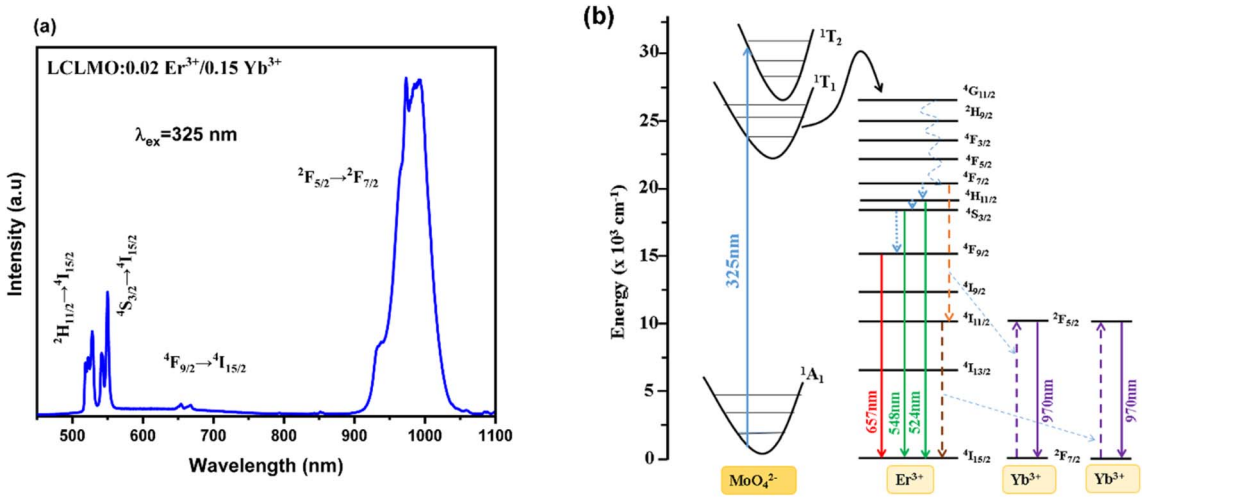

Fig. 2 (a) The emission spectrum at room temperature under 325 nm excitation, (b) schematic energy level diagram of LCLMO doped Er^{3+}/Yb^{3+}.

Er^{3+} ions respectively.[30,31] Under the 325 nm lighting, the molybdate ion is excited from its ground state ($^1A_1$) to the $^1T_2$ state. It then relaxes non-radiatively to a $^1T_1$ state. The energy of the $^1T_1$ state is aligned to the $^4G_{11/2}$ state of the Er^{3+} ion. This allows resonance transfer from molybdate to Er^{3+} without photon emission. In the $^4G_{11/2}$ state, the Er^{3+} ion relaxes non-radiatively to excited levels $^2H_{11/2}$, $^4S_{3/2}$, and $^4F_{9/2}$, emitting green (533 and 553 nm) and red (657 nm) light. This method is referred to as direct excitation (DE) luminescence.

UC luminescence properties

The UC emission spectra of LCLMO:0.02 Er^{3+}/0.15 Yb^{3+} microparticles under 980 nm excitation are illustrated in Fig. 3a. Yb^{3+} ions act as sensitizers, absorbing the 980 nm photons and then transferring the energy to Er^{3+} ions, which behave as activators. The LCLMO:Er^{3+}/Yb^{3+} microparticles show several characteristic UC emission peaks, which can be assigned to the $^2H_{11/2} \rightarrow {}^4I_{15/2}$ (~529 nm) and $^4S_{3/2} \rightarrow {}^4I_{15/2}$ (~545 nm) transitions of Er^{3+} ions, respectively. The corresponding transitions associated with the 529 nm, 545 nm, and 663 ($^4F_{9/2} \rightarrow {}^4I_{15/2}$) nm peaks were discussed previously.[32–34]

The UC luminescence intensities at different pump powers were measured in order to comprehensively investigate the UC luminescence mechanism of the LCLMO:0.02 Er^{3+}/0.15 Yb^{3+} single crystals. It is evident that the green emissions peaks increase steadily as the power increases. Several peaks have been formed in the emission center due to possible energy level splitting. In addition, contour plots of the power-dependent spectra (Fig. S3) have been plotted for comparison:[35,36]

$$I_{UP} = K \times P^n \quad (2)$$

where n is the number of photons necessary for the UC process. The ln–ln plot of the luminescence intensity with the pumping power varying from 5 mW to 30 mW is shown in Fig. S3.

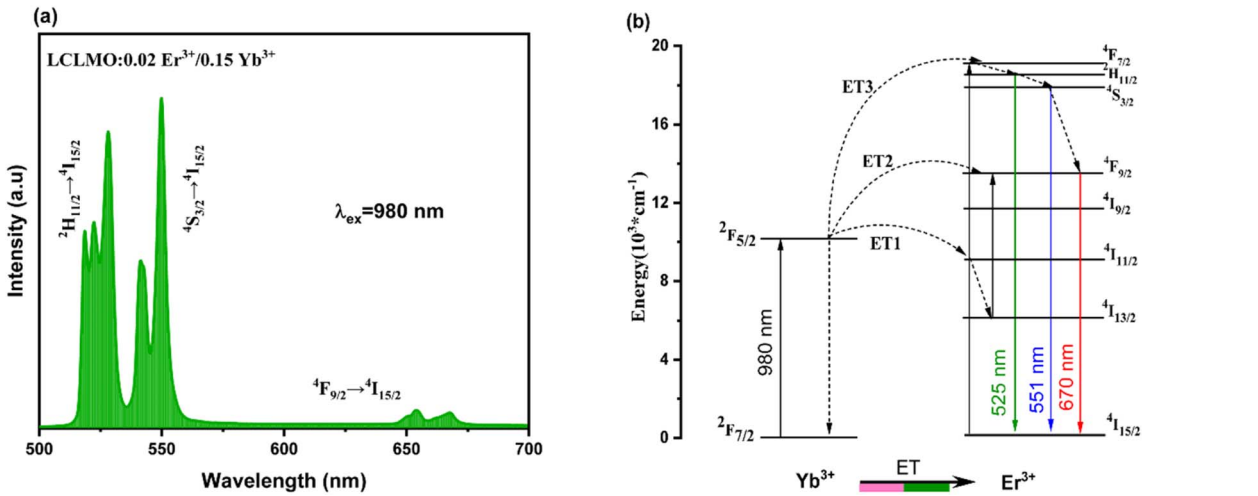

Fig. 3 (a) The UC emission spectrum at room temperature, (b) schematic energy level diagram of LCLMO doped Er^{3+}/Yb^{3+}.

According to the fitting results, the slope correlated with the UC emission of both green and red light is approximately 2. This implies that the generation of the UC emission of both green and red light follows a two-photon process.[37,38]

In order to reveal the UC emission mechanism in LCLMO:0.02 Er^{3+}/0.15 Yb^{3+} phosphors, the corresponding scheme of the main energy transfer process is shown in Fig. 3b. Concisely, after 980 nm optical excitation, the electrons from the $^2F_{7/2}$ ground state are excited to the $^2F_{5/2}$ excited level in Yb^{3+} ions. Following this, the incident energy of the 980 nm radiation is absorbed and transmitted from the Yb^{3+} ions to the corresponding Er^{3+} ions *via* the $^2F_{5/2} + {}^4I_{15/2} \rightarrow {}^2F_{7/2} + {}^4I_{11/2}$ energy transfer (ET) process.[39] This is followed by another ET process from Yb^{3+} to Er^{3+} ions, $^2F_{5/2} + {}^4I_{11/2} \rightarrow {}^2F_{7/2} + {}^4F_{7/2}$, and some part of the electrons populating the $^4I_{11/2}$ level is pumped to the $^4F_{7/2}$ level of the Er^{3+} ions. This is followed by non-radiative (NR) decay, leading to the population in the stark components, the thermally coupled levels (TCLs) of the $^2H_{11/2}$ and $^4S_{3/2}$ excited states, and the stark sublevels of the $^4F_{9/2}$ excited state. Finally, the sample displays the corresponding green and red UC emissions. It is worth noting that the energy separation between the $^2H_{11/2}$ and $^4S_{3/2}$ TCLs is relatively small. So that the transitions from the $^2H_{11/2}$ and $^4S_{3/2}$ excited states to the $^4I_{15/2}$ ground state are thermally coupled, as they are their Stark components. Although, due to the partial overlap of their emission bands, it is necessary to use the Stark sublevels of $^2H_{11/2}$ and $^4S_{3/2}$ to examine the response to temperature changes as well, in order to increase the accuracy of the temperature measurement.[40]

Photometric characterization (CIE)

The Commission International de L'Eclairage (CIE) 1931 standard has been used to estimate the color coordinates of LCLMO:0.02 Er^{3+}/0.15 Yb^{3+} from their respective DC and UC emission spectra, Fig. S4. The color quality and performance of the phosphors are indicated by the CIE coordinates (x, y) in the color space. All coordinates are in the green region of the CIE diagram.[41] The correlated color temperature (CCT) and color purity (CP) for LCLMO:0.02 Er^{3+}/0.15 Yb^{3+} have been estimated from the CIE coordinates in order to accurately determine the visibility of the emission color. The CCT value of a phosphor is the temperature of an ideal black body whose color is almost the same as that of this material. The following empirical McCamy formula was used to calculate the CCT values of all samples.[42]

$$\mathrm{CCT} = -437n^3 + 3601n^2 - 6861n + 5514.3 \quad (3)$$

$$\mathrm{CP} = \frac{\sqrt{(x - x_i)^2 + (y - y_i)^2}}{\sqrt{(x_d - x_i)^2 + (y_d - y_i)^2}} \quad (4)$$

$$n = \frac{(x - x_e)}{(y - y_e)}$$

where $n = (x - x_e)/(y - y_e)$ with (x_e, y_e) the chromaticity epicenter at (0.3320, 0.1858). CP, given by eqn (4) is the average weighting of the resulting CIE coordinates relative to the dominant wavelength coordinates (x_d and y_d) and the coordinate of the point of equal energy (x_i, y_i).

The values obtained for the CIE coordinates, the CCT and the CP are summarized in Table S1. The UC and DC emissions of

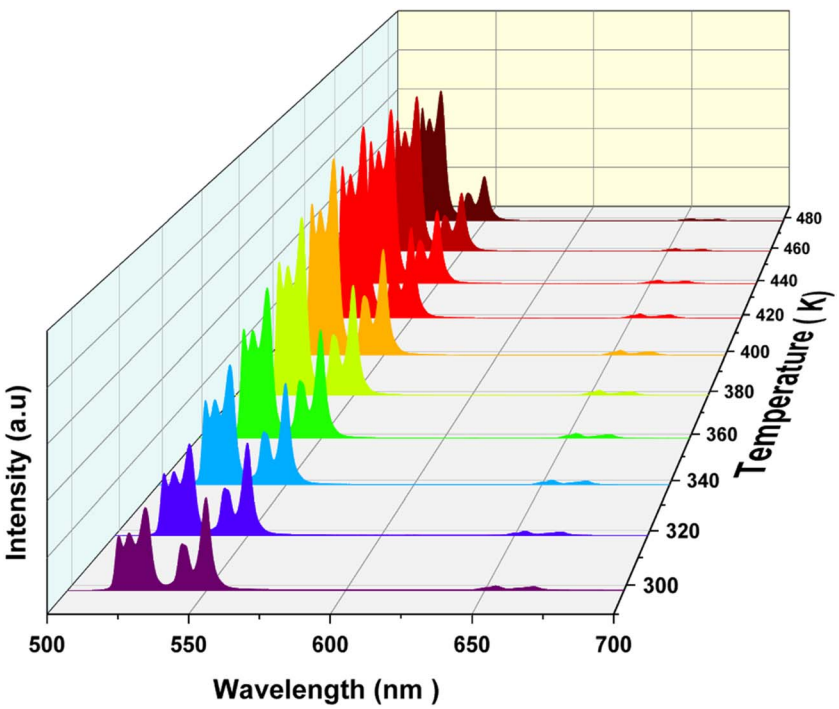

Fig. 4 Temperature dependent down-converted photoluminescence emission spectra of LCLMO:0.02 Er^{3+}/0.15 Yb^{3+} under 325 nm excitation.

the LCLMO:0.02 Er^{3+}/0.15 Yb^{3+} materials both appear in the green region of the CIE diagram, indicating the dominant green emission characteristic of Er^{3+}. In addition, both emissions present high (CCT) (>5000 K), indicating a cool green hue, and excellent CP (>80%), with the UC emission slightly dominant. These results show that the investigated material not only emits bright green light, but also has excellent color purity, making it suitable for optoelectronic applications such as green light-emitting diodes or bio-optical imaging.[43]

Temperature dependent DC luminescence

Typically, temperature has a considerable effect on the spectroscopic properties of luminescent materials. In order to understand the luminescence behavior of the sample more clearly, it is essential to know the actual temperature of the sample (Fig. 4).

On the other hand, it is difficult to realize the accurate temperature measurement of a single point of DC luminescent material by the traditional contact measurement method.[44] It is widely recognized that the optical temperature sensor based on the FIR technique is an effective way to realize non-contact temperature measurement. For Er^{3+} ions, the two green emission levels $^2H_{11/2}$ and $^4S_{3/2}$ belong to the thermally coupled energy levels and it can be used as an optical temperature sensor, in Fig. 5a. According to the Boltzmann distribution, the FIR of the two green emission levels of Er^{3+} ions can be expressed as follows.[45]

$$\mathrm{FIR} = A \exp\left(\frac{-\Delta E}{KT}\right) \tag{5}$$

The red emission's prominence at low excitation power makes it suitable for NTCELs thermometry applications. As a result, the optical thermometric characteristics of Er^{3+} ions at the $^2H_{11/2}$ and $^4F_{9/2}$ levels are investigated under 325 nm excitation (see Fig. 5b). Therefore, conventional FIR is not applicable to NTCLs. Without a well-defined physical model that accurately describes the temperature dependence of the FIR values for Ln^{3+} NTCELs, an empirical approach is crucial for capturing the complex variations observed in the experimental data. The FIR of the two emission levels of Er^{3+} ions can be expressed as follows:

$$\mathrm{FIR} = A \exp\left(\frac{-\Delta E}{KT}\right) + B \tag{6}$$

A is a pre-exponential constant, ΔE is the thermal coupling energy level difference, k_B is the Boltzmann constant, T is the absolute temperature, and B is a constant.

Fig. 5a and b shows the temperature dependent FIR values for the LCMO doped Er^{3+}/Yb^{3+} in the range of 298–473 K. As the temperature increases from 298 to 473 K, the FIR values corresponding to the 526/546 and 526/660 components increase significantly.

For the practical application of temperature sensing, it is essential to investigate the sensor sensitivity in order to quantitatively evaluate its temperature sensing capability. It is well established that there are two commonly used parameters of thermal sensitivity, namely, absolute sensitivity (S_a) and relative sensitivity (S_r). In this study, in order to evaluate the sensitivity of the investigated sample, the following expressions were applied:[45,46]

$$S_r = \frac{1}{\mathrm{FIR}}\left|\frac{\delta \mathrm{FIR}}{\delta T}\right|, \quad S_a = \left|\frac{\delta \mathrm{FIR}}{\delta T}\right| \tag{7}$$

Based on expressions (5) and (7), we observed that the energy gap ΔE between the two thermally coupled levels directly influences the relative thermal sensitivity. Where the absolute thermal sensitivity also depends on ΔE, as well as on the pre-exponential factor B. According to eqn (7), S_a and S_r are calculated and displayed in Fig. 6a and b, of TCLs and NTCLs respectively. The S_a values exhibit an increasing trend with

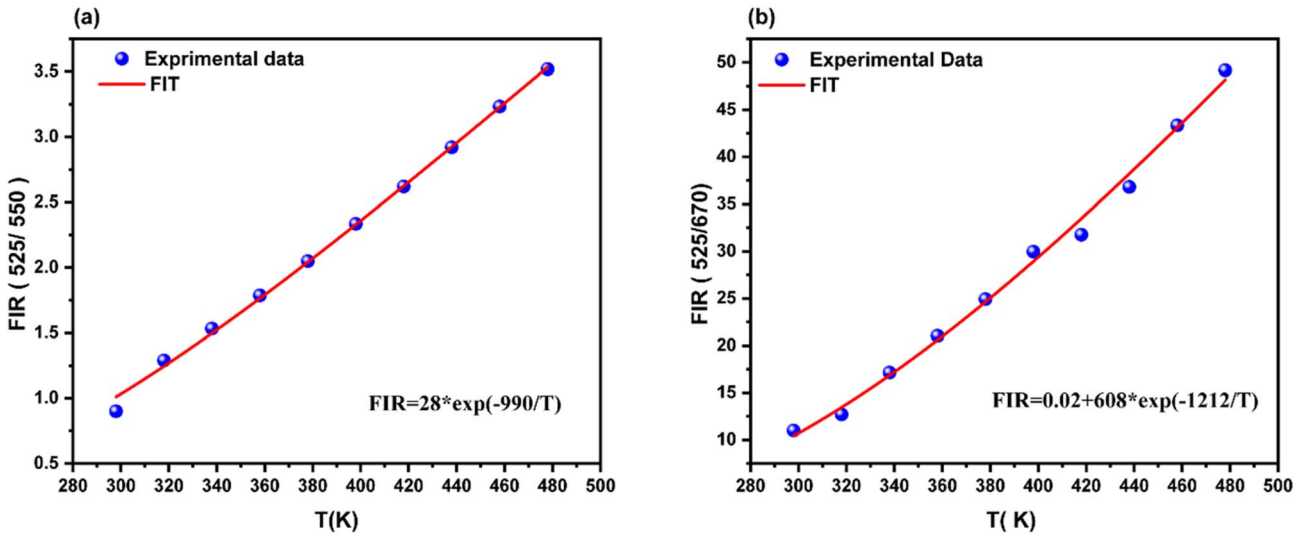

Fig. 5 FIR variation of (a) (I525/I550), (b) (I525/I670) with temperature with 325 nm excitation.

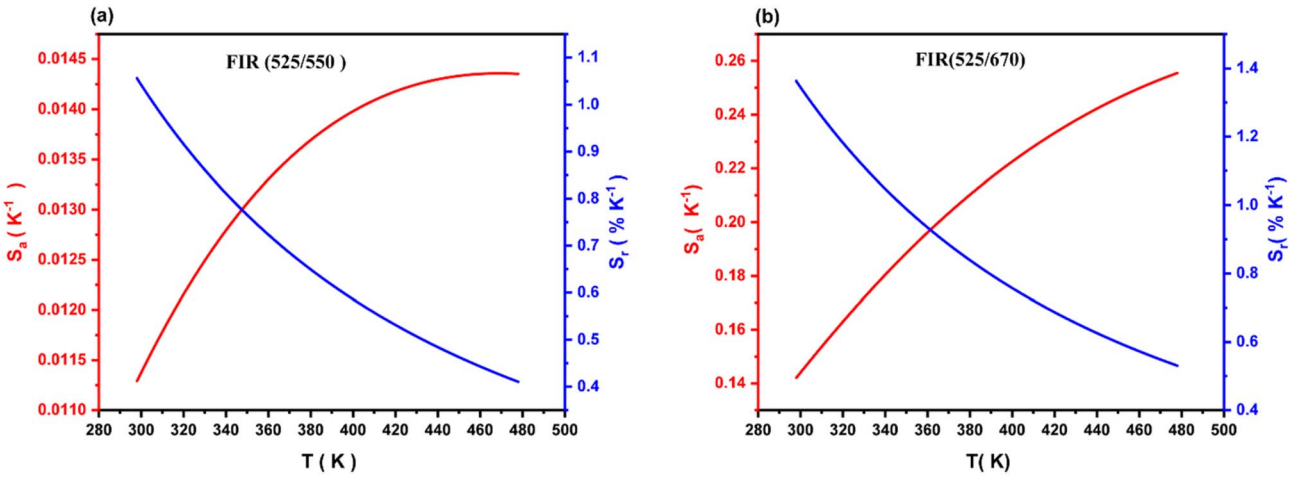

Fig. 6 Absolute sensitivity and relative sensitivity (a) TCL, (b) NTCL for LCLMO:0.02 Er^{3+}/0.15 Yb^{3+}.

increasing temperature from 298 to 473 K, with a maximum values equal to 0.0143 K^{-1} in the TCLs case and 0.25 K^{-1} in the NTCLs case at 473 K. On the other hand, the S_r values exhibit a monotonically decreasing tendency with increasing temperature in the 298 → 473 K temperature range with a maximum values of 1.1% K^{-1} for TCLs and 1.4% K^{-1} for NTCLs at room temperature. However, the results show increasing absolute sensitivity and decreasing relative sensitivity with increasing temperature, reaching their respective maximum values at 473 K for S_a and at room temperature for S_r, with better performance observed in the case of NTCLs. In summary, under 325 nm excitation, the thermally coupled levels ($^2H_{11/2}$ and $^4S_{3/2}$) exhibit predictable Boltzmann behavior, resulting in modest absolute sensitivity and an adequate relative sensitivity. In contrast, the non-thermally coupled ($^2H_{11/2}$ and $^4F_{9/2}$) levels, which are populated *via* temperature-sensitive multiphonon relaxation from higher excited states, exhibit enhanced absolute and relative thermal sensitivities. This emphasizes the significant influence of phonon-assisted energy relaxation on the thermometric performance of NTCL levels for DC processes.

Temperature dependent UC luminescence

To investigate the temperature sensing performance, the temperature-dependent UC emission in the temperature range of 298 K → 460 K was carried out under the 980 nm excitation

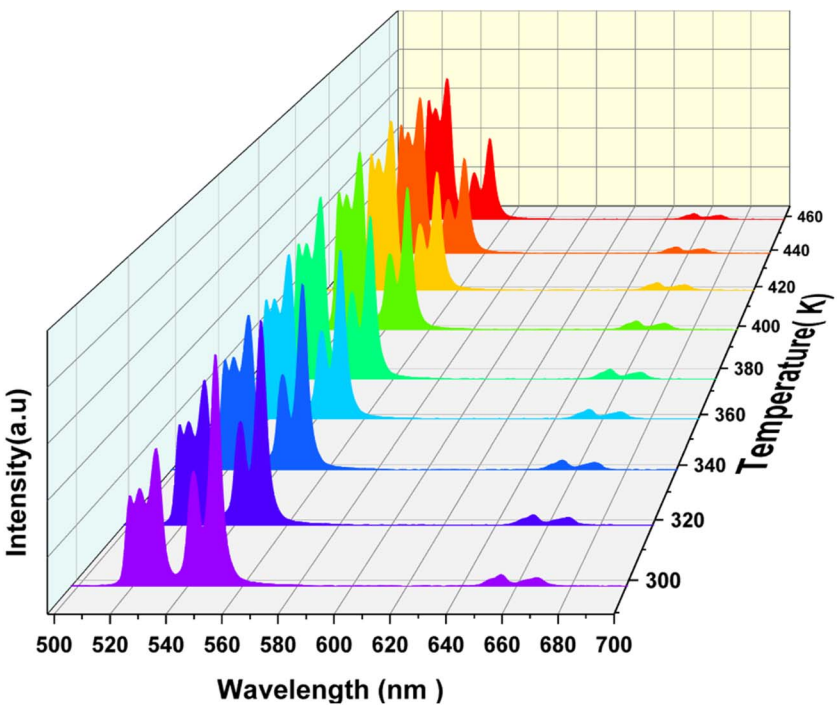

Fig. 7 Temperature dependent UC emission spectra of LCLMO:0.02 Er^{3+}/0.15 Yb^{3+} under 980 nm excitation.

under controlled settings of laser power 20 mW. The intensity of the 525 nm (Er^{3+}: $^2H_{11/2} \rightarrow {}^4I_{15/2}$) band increases and simultaneously the intensity of the 550 nm (Er^{3+}: $^4S_{3/2} \rightarrow {}^4I_{15/2}$) decreases, Fig. 7.[47,48] Increasing temperature has the effect of reinforcing lattice vibrations, increasing the phonon population. This accelerates the non-radiative relaxation between closely spaced energy levels. This process leads to a thermal equilibrium between the energy levels, suggesting that the $^2H_{11/2}$ and $^4S_{3/2}$ states are thermally coupled. The relative population of the two thermally coupled electronic states can be described mathematically using the Boltzmann distribution, as defined in eqn (5).

The evolution of emission intensity with temperature was also examined to evaluate the thermal stability of the $LiCaLa(MoO_4)_3$:Er^{3+}/Yb^{3+} phosphors. Under both UV (325 nm) and NIR (980 nm) excitation, the luminescence intensity initially increases with temperature due to thermally assisted excitation and energy transfer processes. As the temperature approaches 480 K (under UV excitation) and 460 K (under NIR excitation), a moderate decrease in emission intensity is observed, attributed to the onset of thermal quenching. At these temperatures, the intensity decreases by approximately 20% and 10%, respectively. These results confirm that the phosphor exhibits good resistance to thermal quenching and stable luminescent performance across the studied temperature ranges, supporting its potential for practical dual-mode optical thermometry applications.

The change in FIR of TCL and the relative and absolute sensitivities with temperature are shown in Fig. 8a and b, respectively. As shown in Fig. 8c the relative sensitivity decreases with increasing the temperature, exhibiting a maximum at 298 K equal to 1.01% K^{-1}. Besides, the absolute sensitivity increases with increasing temperature with a maximum of 0.0096 K^{-1}. On the other hand, under 980 nm excitation, we observed a significant variation of the $^4F_{9/2} \rightarrow {}^4I_{15/2}$ transition with increasing temperature, which makes it suitable for NTCLs thermometry application. The plots of the absolute and relative sensitivities *vs.* temperature are shown in Fig. 8d. The maximum S_r at 298 K was 0.67% K^{-1}, and the maximum of S_a at 400 K was 0.069 K^{-1}.

It has been demonstrated in this work that the thermal effect induced by the excitation light can be neglected in the down-conversion (DC) luminescence process. In contrast, upconversion (UC) luminescence is significantly influenced by

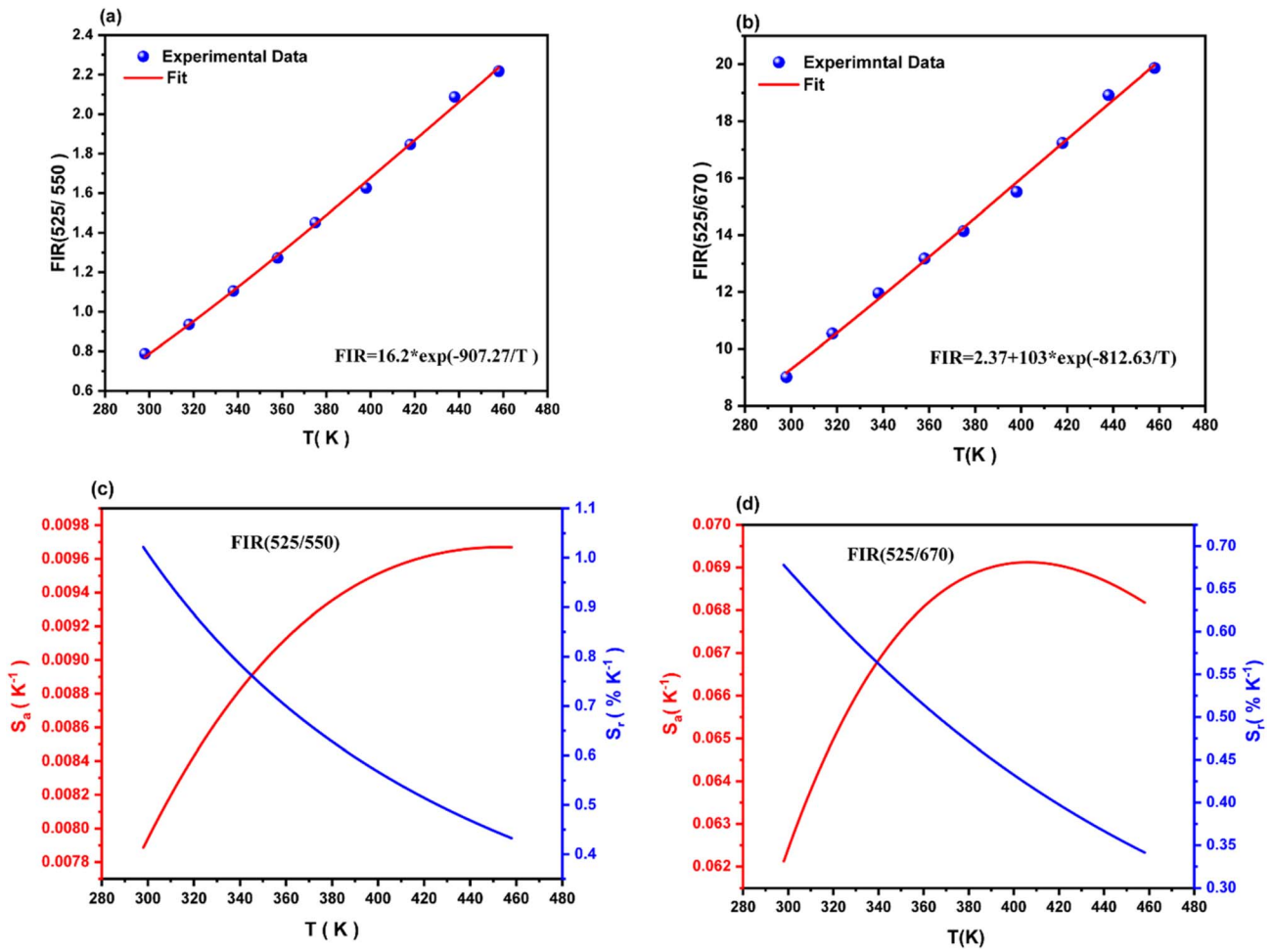

Fig. 8 (a) and (b) FIR variation with temperature. (c) and (d) Absolute sensitivity and relative sensitivity of TCLs (I525/I550), NTCLs (I525/I670), respectively for LCLMO:0.02 Er^{3+}/0.15 Yb^{3+} under 980 nm excitation.

Table 1 Relative thermal sensitivities of different lanthanide doped materials and spectral range of transitions employed

Host	λ_{ex}	T		$S_r(T)$ (% K^{-1})	$S_a(T)$ (K^{-1})	Ref.
$NaGd(WO_4)_2$:Er^{3+}/Yb^{3+}	975	525/550		0.99		52
β-$NaLuF_4$:Er^{3+}/Yb^{3+}	975	303–525		0.42	0.0052	53
LaF_3:Er^{3+}/Yb^{3+}	975	300–515		0.88	0.0016	54
$SrWO_4$:Er^{3+}/Yb^{3+}	975	300–518		0.96	—	55
$Yb_2Ti_2O_7$:Er^{3+}/Yb^{3+}	975	290–610		0.47	—	56
$Na_2GdMg_2(VO_4)_3$:Er^{3+}/Yb^{3+}	975	303–573		0.976	0.07	57
$NaSrY(MoO_4)_3$:Er^{3+}/Yb^{3+}	975	298–335		1.19		58
$YPVO_4$:Er^{3+}/Yb^{3+}	975	300–440		0.937		59
$Ba_2GdV_3O_{11}$:Tm^{3+}/Yb^{3+}	975	303–603		5.397	0.014	60
$NaSrGd(MoO_4)_3$:Er^{3+}	375	298–488		0.87	—	61
$LiCaLa(MoO_4)_3$:Tm^{3+}/Yb^{3+}	975 nm	298–748		1.4	0.4	62
$LiCaLa(MoO_4)_3$:Er^{3+}/Yb^{3+}	325 nm	298–458	TCL	1.05	0.014	This works
	325 nm	298–458	NTCL	1.36	0.25	This works
	980 nm	298–458	TCL	1.01	0.009	This works
	980 nm	298–458	NTCL	0.67	0.069	This works

temperature due to its inherent dependence on phonon-assisted energy transfer processes. As a result, DC-based systems exhibit higher thermal sensitivity and improved thermal resolution. These findings suggest that DC luminescence is more suitable than UC for optimizing the performance of optical temperature sensors, particularly in applications

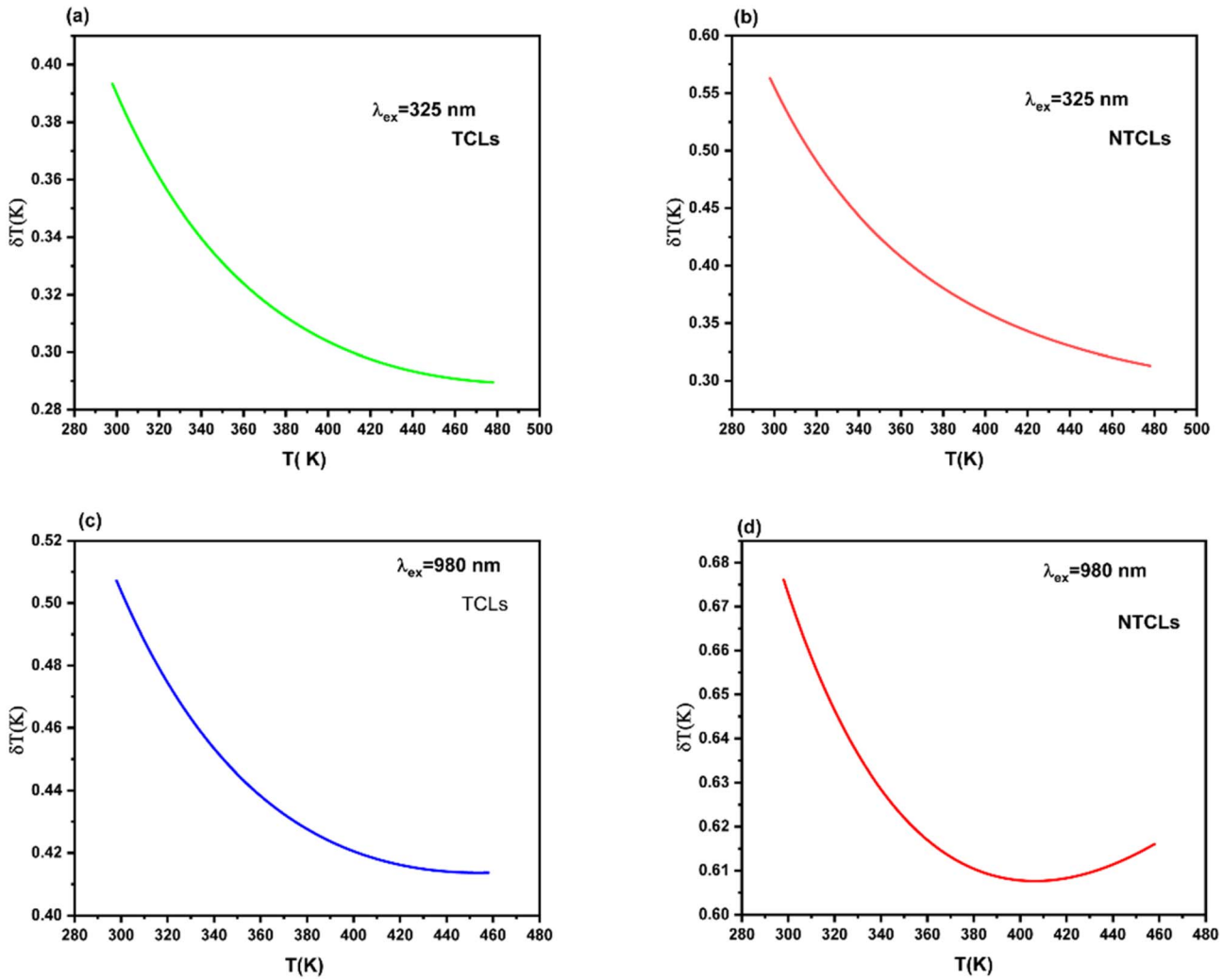

Fig. 9 Temperature uncertainty of LCLMO:Er^{3+}/Yb^{3+}: (a) δT (525/550) nm (down-conversion), (b) δT (525/670) nm (down-conversion), (c) δT (525/550) nm (UP-conversion), (d) δT (525/670) (UP-conversion).

requiring precise and stable thermal detection. Likewise, it was also clearly noted that our phosphor's detection sensitivity, using both UC and DC processes, is higher than many other reported materials, see Table 1. This high sensitivity points to outstanding performance in the field of optical temperature detection.

In order to further investigate the performance of the developed high temperature sensor, we have evaluated the temperature resolution (uncertainty; δT) related to the two band intensities used.[49–51]

$$\delta T = \frac{1}{S_r}\frac{\delta \mathrm{FIR}}{\mathrm{FIR}} \quad (8)$$

where δFIR is the uncertainty of determination of the FIR parameter. In order to assess the limit of detection, also termed as experimental resolution or temperature uncertainty, for LCLMO:0.02 Er^{3+}/0.15 Yb^{3+}, 50 measurements were undertaken under comparable circumstances at room temperature. The standard deviation of the statistical distribution was utilized to establish the uncertainty of the FIR (δFIR) for each approach. In other words, the resultant data were fitted using the Gauss function, and the derived full width at half-maximum (FWHM) of the peaks is equal to the experimental resolution of the sensor. The values obtained are presented in Fig. S5 and S6. According to eqn (8), we calculated the temperature resolutions and displayed them as a function of temperature in the range of 298–478 K. The values obtained are below 1 K, which demonstrates the great accuracy of both FIR methods over the entire temperature range. This finding provides a bare idea of the thermal resolution that can be achieved in temperature measurements using this luminous compound (Fig. 9).

Conclusion

We have successfully synthesized $LiCaLa(MoO_4)_3$ phosphors co-doped with Er^{3+} (0.02) and Yb^{3+} (0.15) *via* a conventional solid-state reaction, and demonstrated their efficient dual-mode photoluminescence under both UV (325 nm) and NIR (980 nm) excitation. The materials exhibit strong green emissions originating from the thermally coupled $^2H_{11/2}$ and $^4S_{3/2}$ levels of Er^{3+}, with co-doping by Yb^{3+} yielding significant enhancement in both DC and UC processes.

Most notably, we have introduced a pioneering dual-mode optical thermometric strategy that simultaneously exploits DC and UC emissions within the $LiCaLa(MoO_4)_3$ host. Over a broad temperature range (300–510 K), the system achieves maximum relative sensitivities of 1.2% K^{-1} (DC) and 2.1% K^{-1} (UC), and maximum absolute sensitivities of 13.6 × 10^{-3} K^{-1} (DC) and 25 × 10^{-3} K^{-1} (UC). The corresponding temperature resolution remains below 0.313 K, underscoring the material's good precision.

These results establish $LiCaLa(MoO_4)_3$:Er^{3+}/Yb^{3+} phosphors is a moderate candidate for advanced luminescent thermometry particularly in non-contact and remote-sensing applications where reliable, high-resolution temperature monitoring is essential.

Conflicts of interest

There are no conflicts to declare.

Data availability

All data underlying the results are available as part of the article and no additional source data are required.

Acknowledgements

I. Mediavilla, and J. Jimenez were partly funded by Spanish Ministry of Science and Innovation (Grants PID2021-126046OB-C22, PID2020-113533RB-C33, TED2021-130786B-I00), and the Regional Government of Castilla y León (Junta de Castilla y León) and by the Ministry of Science and Innovation and the European Union NextGenerationEU/PRTR under the project 'Programa Complementario de Materiales Avanzados'.

References

1 J. Ma, Y. M. Li, W. S. Hu, W. X. Wang, J. C. Zhang, J. H. Yang, *et al.*, *J. Rare Earths*, 2020, **38**, 1039.
2 A. K. Choudhary, A. Dwivedi, A. Bahadur, T. P. Yadav and S. B. Rai, *Ceram. Int.*, 2018, **44**, 9633.
3 R. Dey and V. Kumar Rai, *Methods Appl. Fluoresc.*, 2017, **5**, 015006.
4 C. Zaldo, *Adv. Nanomater.*, 2018, 335–379, DOI: **10.1016/B978-0-12-813840-3.00010-7**.
5 M. D. Dramićanin, A review, *Methods Appl. Fluoresc.*, 2016, **4**, 042001, DOI: **10.1088/2050-6120/4/4/042001**.
6 X. Li, X. Wang, H. Zhong, L. Cheng, S. Xu, J. Sun, J. Zhang, X. Li, L. Tong and B. Chen, *Ceram. Int.*, 2016, **42**, 14710–14715, DOI: **10.1016/j.ceramint.2016.06.096**.
7 N. B. Amar, K. Saidi, C. Hernández-Álvarez, M. Dammak and I. R. Martin, *Mater. Adv.*, 2024, **6**, 827–838.
8 X. T. Ren, J. Gao, H. N. Shi, L. H. Huang, S. L. Zhao and S. Q. Xu, *Optik*, 2021, **227**, 166084.
9 S. Sinha, M. K. Mahata, K. Kumar, S. P. Tiwari and V. K. Rai, *Spectrochim. Acta, Part A*, 2017, **173**, 369–375.
10 X. Wang, X. P. Li, Y. H. Zhang and B. J. Chen, *J. Lumin.*, 2023, **263**, 120055.
11 M. Karampiperi and N. A. Kazakis, *J. Electron.*, 2023, **52**, 5614–5630.
12 F. Paz-Buclatin, F. Rivera-López, O. González, I. R. Martín, L. L. Martin and D. J. Jovanovic, *Sens. Actuators, A*, 2019, **299**, 11628.
13 J. M. MarquesdeSouza, K. d. O. Lima, J. L. Ferrari, L. J. Q. Maia, R. Rocha Goncalves, R. F. Falci and D. Manzani, *Dalton Trans.*, 2022, **51**, 4087–4096.
14 X. Gao, F. Song, D. Ju, A. Zhou, A. Khan, Z. Chen and L. Liu, *CrystEngComm*, 2020, **22**(42), 7066–7074.
15 S. Balabhadra, M. F. Reid, V. Golovko and J. P. R. Wells, *Opt. Mater.*, 2020, **107**, 110050.
16 L. Mariscal-Becerra, V. M. Velazquez-Aguilar, M. C. Flores-Jimenez, D. Acosta-Najarro, V. Torres-Zuniga, R. Vaquez-

Arreguín and C. Falcony-Guajardo, *J. Alloys Compd.*, 2020, **846**, 156295.
17 J. Ma, Y. Hu and L. Liu, *Natl. Sci. Rev.*, 2025, **12**, nwae099, DOI: 10.26599/NR.2025.94907097.
18 Z. Zhang, Z. Wang, M. Zhang, T. Sun, Y. Sun, H. Ye, J. Shi, Z. Wei, S. Jin and L. Zhang, *Nat. Commun.*, 2022, **13**, 2233, DOI: 10.1038/s41467-022-29784-6.
19 N. El-Amassy, T. M. Zayed, M. Abdel-Baki and E. A. El-Diasty, *Opt. Mater.*, 2024, **150**, 115144, DOI: 10.1016/j.optmat.2024.115144.
20 D. Wu, J. Li, H. Huang, T. Liu, C. Yang, Y. Zhao, S. Lu, Z. Liu and H. Zhang, *J. Mater. Chem. C*, 2025, **13**, 15426–15441, DOI: 10.1039/D5TC00404G.
21 Y. Bahrouni, I. Kachou, K. Saidi, T. Kallel, M. Dammak, I. Mediavilla and J. Jiménez, *Mater. Adv.*, 2025, **6**, 1307–1318.
22 K. Saidi, M. Yangui, C. H. Álvarez, M. Dammak, I. R. M. Benenzuela and M. Runowski, *ACS Appl. Mater. Interfaces*, 2024, **16**, 19137–19149, DOI: 10.1021/acsami.4c00313.
23 V. Naresh and N. Lee, *Mater. Sci. Eng., B*, 2021, **271**, 115306.
24 K. Saidi, C. Hernández-Álvarez, M. Runowski, *et al.*, *Dalton Trans.*, 2023, **52**, 14904–14916, DOI: 10.1039/d3dt02613b.
25 P. K. Vishwakarma, S. B. Rai and A. Bahadur, *Mater. Res. Bull.*, 2021, **133**, 111041.
26 P. Kaczorowska, D. Hreniak, A. Bieńko, A. Bednarkiewicz and W. Strek, *J. Lumin.*, 2018, **200**, 59–65.
27 M. Runowski, D. Woźniak, J. Zychowicz, S. Lis and L. Marciniak, *J. Mater. Chem. C*, 2021, **9**, 4643–4651.
28 P. Sharma, J. P. Madda and S. Vaidyanathan, *Dalton Trans.*, 2023, **52**(41), 15043–15056, DOI: 10.1039/D3DT02716C.
29 B. P. Singh, A. K. Parchur, R. S. Ningthoujam, A. A. Ansari, P. Singh and S. B. Rai, *Dalton Trans.*, 2014, **43**, 4770–4778.
30 J. Zhang, Y. Liu, L. Li, N. Zhang, L. Zou and S. Gan, *RSC Adv.*, 2015, **5**(37), 29346–29352.
31 A. Kumar and J. Manam, *J. Alloys Compd.*, 2020, **829**, 154610.
32 A. Prasad, A. S. Rao and G. V. Prakash, *Mol. Struct.*, 2020, **1205**, 127647.
33 C. S. Lim, *et al.*, *Crystals*, 2023, **13**(2), 362.
34 S. Tabanli and G. Eryurek, *Sens. Actuators, A*, 2019, **285**, 448–455.
35 S. Tomar, N. K. Mishra, V. Kesarwani, V. K. Rai, K. Kumar and C. Shivakumara, *ACS Appl. Opt. Mater.*, 2024, **2**, 1965–1984.
36 C. S. McCamy, *Color Res. Appl.*, 1992, **17**, 142–144.
37 K. Saidi, I. Kachou, K. Soler-Carracedo, M. Dammak and I. R. Martín, *ACS Appl. Nano Mater.*, 2023, **6**, 17681–17690.
38 X. Li, B. Bao, X. He, G. Wang, Y. Huang, L. Li and Y. Yu, *J. Mater. Chem. C*, 2023, **11**, 2494–2504.
39 H. Lv, Q. Wu, L. Luo, W. Li and P. T. Du, *J. Phys. Chem. C*, 2023, **127**(7), 3808–3818.
40 M. Runowski, S. Goderski, D. Przybylska, T. Grzyb, S. Lis and I. R. Martín, *ACS Appl. Nano Mater.*, 2020, **3**(7), 6406–6415.
41 Z. Rao, Q. Li, Z. Li, L. Zhou, X. Zhao and X. Gong, *J. Phys. Chem. Lett.*, 2022, **13**, 3623–3630.
42 S. Liu, H. Ming, J. Cui, S. Liu, W. You, X. Ye and R. Wang, *J. Phys. Chem. C*, 2018, **122**(28), 16289–16303.
43 G. T. Jasso, E. Montes, J. G. Olguín, D. S. Guzmán, R. L. Esquivel, I. R. Martín and J. G. Mendoza, *Ceram. Int.*, 2018, **44**(1), 154–157.
44 Z. E. A. Taleb, M. Dammak, I. Kachou, K. Saidi, I. Mediavillac and J. Jiménezc, *Mater. Adv.*, 2025, **6**, 2385.
45 H. Suo, X. Zhao, Z. Zhang, Y. Wu and C. Guo, *ACS Appl. Mater. Interfaces*, 2018, **10**, 39912–39920.
46 V. Kesarwani and V. K. Rai, *J. Appl. Phys.*, 2022, **132**, 113102.
47 B. Lei, L. Lu, F. Hu, L. Ning, D. Shao, H. Sun, X. Zhang, Z. Bai and X. Mi, *J. Lumin.*, 2022, **251**, 119123.
48 C. Hernández-Alvarez, G. Brito-Santos, I. R. Martín, J. Sanchiz, K. Saidi, K. Soler-Carracedo, Ł. Marciniak and M. Runowski, *J. Mater. Chem. C*, 2023, **11**(30), 10221–10229.
49 P. Du, L. Luo, H.-K. Park and J. S. Yu, *Chem. Eng. J.*, 2016, **306**, 840–848.
50 K. Shwetabh, N. K. Mishra and K. Kumar, *Mater. Sci. Semicond. Process.*, 2023, **167**, 107806.
51 Sonali Tomar and C. Shivakumara, *Methods Appl. Fluoresc.*, 2023, **11**, 024001.
52 J. Liao, L. Nie, Q. Wang, S. Liu, H.-R. Wen and J. Wu, *RSC Adv.*, 2016, **6**(42), 35152–35159.
53 K. Zheng, W. Song, G. He, Z. Yuan and W. Qin, *Opt. Express*, 2015, **23**, 7653–7658.
54 X. Cheng, X. Ma, H. Zhang, Y. Ren and K. Zhu, *Phys. B*, 2017, **521**, 270–274.
55 A. Pandey, V. K. Rai, V. Kumar, V. Kumar and H. C. Swart, *Sens. Actuators, B*, 2015, **209**, 352–358.
56 B. S. Cao, Y. Y. He, Z. Q. Feng, Y. S. Li and B. Dong, *Sens. Actuators, B*, 2011, **159**, 8–11.
57 L. Li, Y. Tong, J. Chen, Y. Chen, G. AbbasAshraf, L. Chen, T. Pang and H. Guo, *J. Am. Ceram. Soc.*, 2022, **105**(1), 384–391.
58 K. Saidi, C. Hernández-Álvarez, M. Runowski, M. Dammak and I. Rafael Martín Benenzuela, *ACS Appl. Nano Mater.*, 2023, **6**(20), 19431–19442, DOI: 10.1021/acsanm.3c04031.
59 F. Ayachi, K. Saidi, M. Dammak, W. Chaabani, I. Mediavilla Martínez and J. Jiménez, *Mater. Today Chem.*, 2023, **27**, 101352, DOI: 10.1016/j.mtchem.2022.101352.
60 I. Kachou, K. Saidi, M. Dammak, C. Hernández-Álvarez and I. R. Martın, *Mater. Adv.*, 2024, **5**, 8280.
61 Z. E. A. A. Taleb, K. Saidi and M. Dammak, *RSC Adv.*, 2024, **14**, 8366.
62 I. Kachou, K. Saidi, Z. E. A. A. Taleb, C. Hernández-Álvarez, M. Dammak and I. R. Martín, *Mater. Adv.*, 2025, DOI: 10.1039/D5MA00489F.